Journal of Porous Materials (2022) 29:1011–1025
https://doi.org/10.1007/s10934-022-01230-4

Graphene aerogel and its composites: synthesis, properties and applications

Ashish K. Kasar[1] · Siyu Tian[1,2] · Guoping Xiong[1,2] · Pradeep L. Menezes[1]

Accepted: 1 March 2022 / Published online: 16 March 2022

Abstract
Graphene is an attractive material for many applications due to excellent inherent properties such as lower density, high mechanical strength, higher thermal conductivity, etc. However, it has been used as an additive material due to size limitation. To overcome the size limitation without affecting the inherent properties of 2D graphene sheets, researchers have developed graphene aerogel (GA) by different synthesis techniques. GA has become an emerging light-weight structure in the group of aerogel materials because of various applications. In this review article, the mechanical properties of GA have been discussed by considering the structural parameters of GA, such as pore size, graphene sheet alignments, and wall thickness, because the mechanical performance of the GA is an important criterion prior to its application in any field. It has also been highlighted that the structural parameters can be altered during synthesis to achieve desired mechanical properties. Applications of GA have been thoroughly discussed in the field of polymer composites and how GA-polymer structures can help to generate a cleaner environment by separating spilled oil from water and removing organic pollutants from water. In addition, potential of GA for various other applications with suitable nano material additives have been highlighted.

Keywords Graphene aerogel · Hydrothermal · Freeze-casting · Compressive stress

Abbreviations

GA	Graphene aerogel
GO	Graphene oxide
GH	Graphene hydrogel
rGH	Reduced graphene oxide hydrogel.
PDMS	Polydimethylsiloxane
PDA	Polydopamine
APTS	3-Aminopropyltriethoxysilane
PMMA	Poly methyl methacrylate
BPA	Bisphenol A
MO	Methyl orange
g-C_3N_4	Graphitic carbon nitride
DSSC	Dye sensitized solar cell
PEG	Polyethylene glycol
COF	Coefficient of friction

✉ Guoping Xiong
gxiong@unr.edu

✉ Pradeep L. Menezes
pmenezes@unr.edu

[1] Department of Mechanical Engineering, University of Nevada, Reno 89557, USA

[2] Department of Mechanical Engineering, The University of Texas at Dallas, Richardson, TX 75080, USA

1 Introduction

Graphene is a single atomic layer of carbon that contains excellent physical, mechanical, thermal, and electronic properties. Graphene was first synthesized in 2004 by the scotch tape method [1]. From then, graphene has achieved attraction from all the fields, leading to the synthesis of graphene by various other methods such as chemical exfoliation, mechanical exfoliation, thermal decomposition of carbon compounds, and chemical vapor deposition detailed in prior review articles [2, 3]. Graphene has superior properties, which are listed in Table 1 and compared with other suitable materials. For example, Young's modulus of graphene was observed to be ~ 1000 GPa [4], which is five times higher than steel. Similarly, thermal conductivity of graphene is ~ 5000 W/m/K [5], which is enormously higher than that (398 W/m/K) of copper [6]. Graphene also has large specific surface area (2600 m^2/g) [7].

The direct application of graphene is restricted due to its nano size, difficulty to produce in large quantity and superior quality (defect-free structure). The properties of graphene are being utilized in the form of composites. For example, improved mechanical properties of the metal composites with graphene have been observed by the uniform

Table 1 Properties of graphene compared to other materials

Properties	Graphene	Other materials with properties
Density	1.5–2.0 gm/cm^3 [8]	Lithium: 0.534 gm/cm^3
Young's modulus	~1000 GPa [4]	Steel, ASTM A36: 200 GPa [9]
Tensile strength	130 GPa [4]	Steel, ASTM A36: 200 GPa [9]
Thermal conductivity	~5000 W/m/K [5]	Cu annealed: 398 W/m/K [6]
Specific surface area	2630 m^2/g [10]	Porous activated carbon: 3164 m^2/g [11]
Optical transmittance	~97.7% [12]	indium tin oxide: 94.8% [13]
Current density	10^8 Å/cm^2 [14]	Cu: 82–98 × 10^6 Å/cm^2 [15]
Fermi velocity	c/300 = 1,000,000 m/s [16]	Monolayer borophene: 3.5 × 10^6 m/s [17]

distribution of graphene nanoparticles in the metal matrix [18, 19] or by the synthesis of the alternating layer of metal/graphene [20]. Graphene composites have also been studied as an electrode for electrochemical energy storage applications. Chou et al. [21] synthesized the Si/graphene electrode for a reversible lithium battery. The authors found that the Si/graphene composite maintained a capacity of 1168 mAhg^{-1} after 30 cycles, whereas pristine Si electrode showed a drastic drop in capacity from 3026 to 346 mAhg^{-1} after 30 cycles. The higher discharge capacity of the Si/graphene electrode was observed due to the good electrical contact provided by graphene. Also, the higher surface area and porous nature of graphene helped to achieve easy access to electrolytes.

The surface area of the graphene plays a significant role in the improvement of the properties. The surface area of graphene can be utilized by the formation of graphene aerogel (GA). Aerogel is a porous structure that is synthesized using a gel where a liquid component of the gel is replaced by gas, generally air. Aerogels of various other materials such as silica [22], carbon [23, 24], alumina [25–27], titania [28], and zirconia [29, 30] have been studied which has applications as a catalyst, adsorbent, thermal insulation, etc. In addition, composite aerogels have also been studied for different applications. For example, Pt/titania aerogel for hydrogen evolution by photocatalyst water splitting [31], titania-silica aerogel for degradation of glyphosate [32], alumina-silica aerogel for absorption [33] and alumina-ZrC-carbon aerogel for thermal insulation [34] etc. In comparison with these aerogel materials, GA is superior because it consists of two-dimensional atomic layers which provides maximum specific surface area. In addition, inherent properties of carbon make it suitable for various applications including electrochemical energy storage, water cleaning, etc.

The most common method of aerogel synthesis is the hydrothermal process followed by a freeze-casting method where aqueous graphene oxide (GO) solution placed in a Teflon-lined autoclave at 120–180 °C and up to 1 MPa to achieve hydrothermal condition [35, 36]. The hydrothermal conditions lead to cross-linking of GO sheets by removal of oxygen carrying functional groups such as −OH and −COOH. The removal of these functional groups and cross-linking yield reduced graphene oxide hydrogel (rGH). Therefore, the process is also called hydrothermal reduction. The rGH can be naturally dried to obtain GA. However, the preferred drying method is freeze-drying, where ice is formed due to the freezing process, and it sublimates under vacuum and leaves a negative replica of ice crystals as GA [36, 37]. The process of hydrothermal and freeze-drying is shown in Fig. 1a. The temperature gradient can be controlled during freezing to achieve the directional growth of graphene sheets in the aerogel [38, 39]. Therefore, the morphology of the GA formed by the freeze-drying method depends on the nucleation and growth of ice crystals. Some studies also reported annealing of as prepared GA in the temperature range of 400 °C to 2500 °C [40, 41]. The improvement in mechanical properties due to thermal reduction during annealing is discussed in the next section.

3D printing has also been successfully utilized to synthesize the GA that involves GO solution with suitable rheological properties. A schematic of GA synthesis by 3D printing is shown in Fig. 1b. The rheological properties of the ink can be adjusted by suitable additives such as $CaCl_2$ and silica. This GO solution, also called GO ink, is extruded through a micro nozzle and printed in the air [42, 43] or specific solution such as isooctane [44]. Then, the deposited structure is freeze-dried and thermally reduced to obtain 3D printed GA.

Applications of GA can require specific properties that can be achieved or enhanced by using suitable synthesis techniques to control wall thickness, pore size, etc. In addition, modification in graphene, including functionalization or doping of different elements or compounds, can be carried out during the synthesis of GA. Therefore, it is important to understand the available synthesis technique of GA and possibly physical or chemical modification. In this review article, the effect of different synthesis parameters on the mechanical properties of GA has been discussed because the mechanical strength of GA is an important consideration for possible applications. The applications of GA in the field of solid polymer composite and porous GA-polymer composite are also discussed.

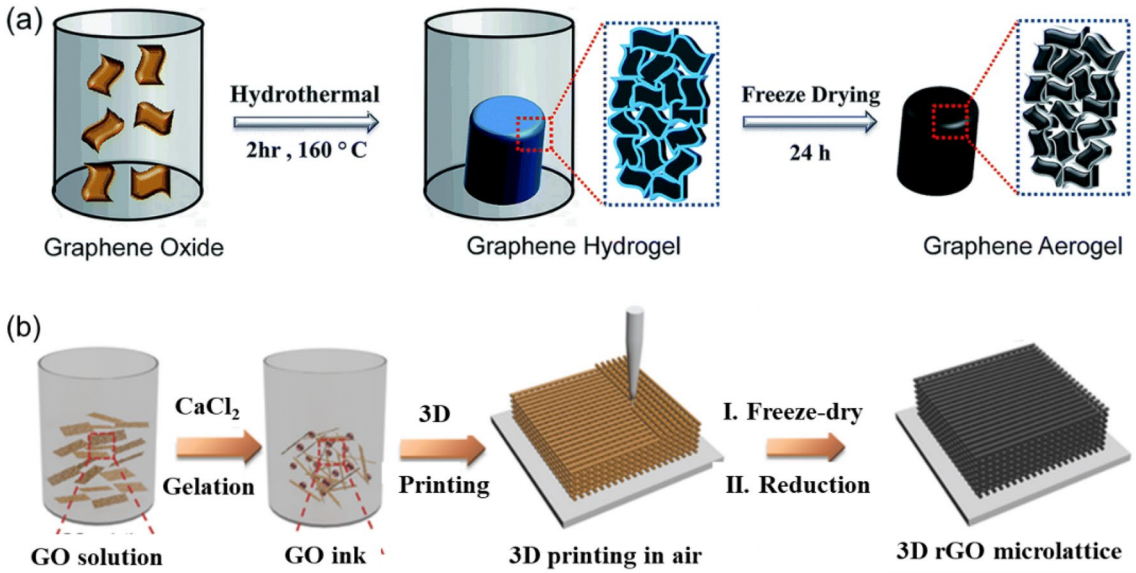

Fig. 1 GA synthesis by **a** hydrothermal + freeze-drying (Reproduce with permission [45]) and (b) 3D printing + freeze-drying (Reproduce with permission [43])

2 Mechanical properties of GA

Mechanical performance of GA depends on various factors, including pore size, graphene flake size, pore volume, etc. The mechanical strength of GA is mostly evaluated by compression testing. Gao et al. [46] studied the effect of flake size on mechanical properties. The authors used GO flakes with sizes of 50, 20, and 1 µm to form GA by hydrothermal and freeze-drying methods. Larger flake sized GA was observed to have higher strength, modulus, and fatigue resistance. It was hypothesized that the larger flake size provides more resistance to the slip between adjacent flakes during deformation. Thus, it improves mechanical properties. The mechanical strength of GA also depends on the synthesis technique that controls the microstructure characteristics of the aerogel, including structural geometry and pore size. Different studies have been listed in Table 2 on the mechanical performance of GA along with their structure, pore size, and synthesis technique. For example, studies [47] and [48] listed in Table 2 show that GA with lamellar structure synthesized by freeze-casting have different pore size that resulted in significant difference in mechanical properties. More specifically, GA with smaller pore sizes (10–30 µm) has higher compressive strength compared to GA with a pore size of 100 µm.

The mechanical strength of the GA depends on the interaction between graphene sheets in the aerogel structure, which can be controlled during synthesis. The effect of graphene sheet interaction was monitored by Han et al. [49]. The authors synthesized the GA by hydrothermal method followed by freeze-drying at − 60 °C. Prior to the freeze-drying process, the prepared graphene hydrogel (GH) was kept in ammonia solution (14 v/v%) at 25, 60, and 90 °C for 1 h to replace the water content. After freezing at − 60 °C, ice crystals were seen on the non-treated samples, whereas the ammonia treated sample did not show ice. The absence of ice confirmed that the water was replaced by ammonia solution. The formation of ice led to broken GA due to expansion from water to ice. Whereas, a stable structure was obtained for ammonia treated GA. It suggests that ammonia solution helps to retain the structure. Moreover, a higher compressive strength was observed for GA with ammonia treatment at 90 °C. The Fourier transform infrared spectroscopy analysis on ammonia-treated GA showed peaks of oxygen and nitrogen containing functional groups which were quantified using X-ray photoelectron spectroscopy in terms of elemental ratio between carbon–oxygen (C/O) and nitrogen/carbon (N/C). The ammonia-treated GA had a higher C/O ratio (7.46) as compared to that (4.31) of untreated GA, and nitrogen was observed in ammonia-treated GA with N/C ratio of 0.05. The increase in C/O and N/C ratio suggests that more covalent bonds between graphene sheets increased the compressive strength. Similarly, other graphemes based composite aerogels have been studied, which are listed in Table 3 along with the pore size, solvent and sorption capacity.

The freezing temperature also affects the morphology of GA. As explained earlier, the freezing temperature affects the nucleation sites for ice crystallization, i.e., a lower temperature will result in a higher number of nucleation sites and lesser growth that will affect the pore size in GA during freeze-drying. This effect was studied by Zhu et al. [39] by

Table 2 Mechanical properties of GA

Material	Structure	Pore size	Elasticity	Compressive stress	Synthesis technique	Refs.
GF	Spherical	60 µm	99%	5.4 MPa at 99%	Freeze drying	[53]
GF	Random	Submicron-5 µm	–	24 kPa yield stress	Hydrothermal	[35]
GF	Honeycomb	50 ± 0.2 µm	87%	E = 300 kPa	Microfluidic	[54]
GF	Honeycomb	100–300 µm	99%	14.5 m^2/g	Freeze drying	[55]
GF	Honeycomb	50 µm	0.12 Scm^{-1}	18 kPa at 80% strain	Freeze-casting	[56]
GF	Random	166 F/g at 10 mV/s	87 S/m	E = 0.13 MPa	Chemical reduction	[40]
GF	Spherical	~ 100 µm, 490 m^2/g	99%	42.3 kPa	Hydrothermal	[57]
GF	Interconnected		90%	12.8 kPa	Dip-coating	[58]
GF	Random		90%	~ 20 kPa	Chemical Reduction	[59]
GF	Ordered	15 µm	60%	5.88 kPa	Hydrothermal	[60]
GF	Periodic	1066 m^2/g	90%	11 MPa	3D printing	[44]
GF	Lamellar	~ 100 µm	50%	3 kPa	Freeze-casting	[47]
GF	Lamellar	10–30 µm, 45.6 m^2/g	90%	134.1 kPa	Freeze-casting	[48]
GF	Lamellar	> 50 µm, 51.4 m^2/g	90%	105 kPa	Freeze-casting	[61]
GF	Lamellar	400 m^2/g, 11–30 µm	10%	7.7 kPa	RT Freeze-casting	[62]
NDGA	Honeycomb	160 m^2/g, 100–200 µm	99%	1.6 MPa	Hydrothermal + freezing	[63]
GPO foam	Randomly	30 µm	80%	0.28 MPa	Sol–gel	[64]
GF	Randomly	854 m^2/g, 2–100 nm	80%	9 MPa	Sol–gel	[65]
SGF	Spherical	40–120 µm	99%	5.4 MPa	Freeze-casting	[53]
	Randomly		98%	80 kPa	Solvothermal	[36]
GM	Honeycomb	20–50 µm	99%	0.71 MPa	Hydrothermal + freezing	[66]

Table 3 Various graphene composite aerogel material with their oil–water separation capacity

Aerogel material	Pore size	Solvent	Sorption capacity	Refs.
Graphene/polyvinylidene fluoride	3.4–100 nm	Organic solvents and oil	5–200 (wt/wt)	[84]
Graphene/polydomine/chitosan	4–40 nm	Organic solvent and oil	10–20 (wt/wt)	[75]
Graphene /polystyrene/Fe_3O_4	–	Diesel and crude oil	30–40 (wt/wt)	[74]
Graphene/cellulose nanofiber	5–10 µm	Organic solvent	200–700 (wt/wt)	[85]
Graphene	3.8–109 nm	Organic solvent and oil	100–130 (wt/wt)	[86]
Alginate/grapheme oxide aerogel	50–150 µm	Vegetable and mineral oils	98.5–99.5% (separation efficiency for 1:1 oil-sea water mixture)	[87]
Carbon nano tube/graphene	2–100 nm	Organic solvent and mineral oil	120–330 (wt/wt)	[88]
Lignin-modified graphene	50–200 µm	Organic solvent and oil	200–350 (wt/wt)	[89]
Fluoroalkyl silane functionalization	Meso and micropores	Mineral and vegetable oil	50–70 (g/g)	[45]
Polyvinyal alcohol-GA	50–70 µm	n-hexane, cyclo-hexane, diesel, toluene, methyl benzoate, dichloromethane and carbon tetrachloride	114–286 (g/g)	[90]
Enteromorpha-GA	8–9 nm	Oil and organic solvents	68–200 (g/g)	[91]

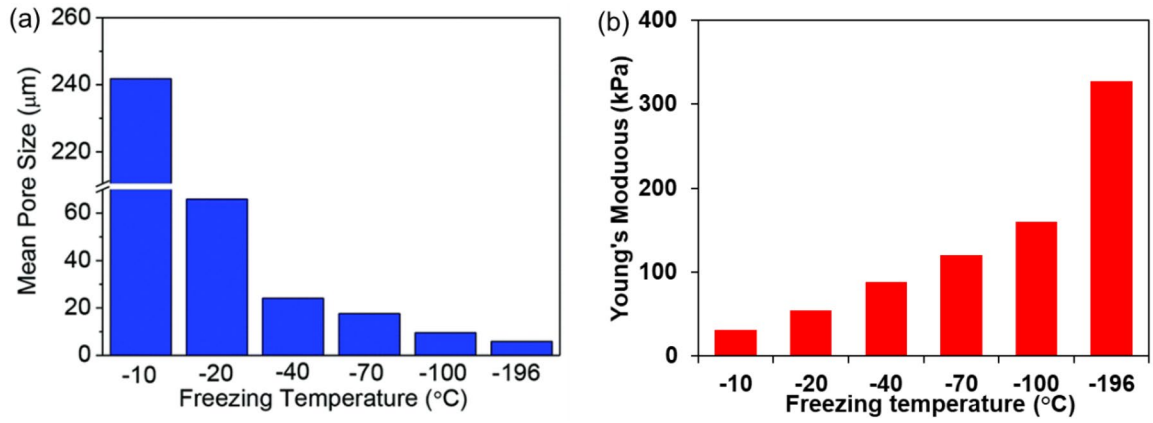

Fig. 2 Effect of freezing temperature on **a** Mean pore size in GA and **b** Young's modulus. Reproduce with permission [39]

freezing GA at different temperatures from – 10 to – 196 °C. The effect of freezing temperature on the pore size is shown in Fig. 2a that shows the largest pore size at freezing temperature of – 10 °C due to ice crystal growth and smallest pore size of 5.9 μm was observed for a freezing temperature of – 196 °C. The morphology of the GA structure also changed: rod-like structure at – 10 °C, tube-like structures at – 20, and – 40 °C and uniform refined morphology at – 196 °C due to change in ice crystallization from dendritic to equiaxed crystals. The values of Young's modulus were retrieved from the study and plotted in Fig. 2b against the freezing temperature. As expected, Young's modulus increased with a decrease in pore size of the GA.

In addition to freezing temperature, the effect of GO content during the hydrothermal synthesis of GA was extensively investigated by Liu et al. [50]. The reduced GA was prepared with different concentrations of GO (2, 4, 6, 8, 10, 15 and 30 mg/ml) and at different freezing temperatures (– 5, – 20, – 40, – 60, – 80 and – 196 °C). The effect of these parameters was observed in terms of pore size, density, wall thickness, and mechanical properties, as illustrated in Fig. 3. Young's modulus and wall thickness were observed to increase with density (Fig. 3a). In contrast, maximum recovery and minimum energy loss coefficient were observed for a lower density of 4 mg/cm^3 (Fig. 3b). However, Young's modulus and energy loss coefficient were observed to decrease with pore size (Fig. 3c and d). The mechanical performance of GA is summarized in Fig. 3e with four regions. The region (I) shows ultra-flyweight with lower GO content that yields lower density and poor mechanical performance due to interfacial adhesion in the ultrathin walls. The region (II) shows the GA with super elasticity and low energy loss coefficients where π–π interaction between sheets strengthens the structure. GA in the region (III) with a relatively higher GO content results in thicker wall that resists deformation (higher modulus) but lesser recovery after compression. GA with the highest strength and modulus belongs to the region (IV) due to increased wall thickness.

GA, formed by 3D printing, has an advantage of dilute precursor GO solution that is used as ink, provides lower density compared to the convention GA. For example, Zhu et al. [44] compared the compressive stress–strain curves for conventional GA (31 mg/cm^3), and 3D printed GA with GO ink (16 mg/cm^3), shown in Fig. 4a and b, respectively. By comparing the unloading curves, it can be seen that the 3D printed GA has less permanent residual deformation and slightly higher recoverability compared to conventional GA due to a lower density and open structure. The authors also modified the GO ink with organic sol–gel chemistry by adding resorcinol and formaldehyde in GO ink to build an open and lesser crosslinked network. The stress–strain curve for 3D printed GA with modified GO ink (density: 53 mg/cm^3) is shown in Fig. 4d, which is compared with conventional GA with sol–gel chemistry (density: 123 mg/cm^3). Both the crosslinked GA shows extraordinary super compressibility with full recovery even after 50% of strain. A similar higher recovery under compressive strains was observed by other researchers [42, 43]. In addition to crosslinking additives, different additives such as graphene nanoplatelets, SiO_2, Ag nanoparticle, carbon nanotubes, MoS_2 have been added in the GO ink to achieve superior electrical, electrochemical properties of the 3D printed GA [51, 52].

These studies show that the GA can be tailored to achieve desired mechanical properties (strength and resilience) by modifying the structural parameters including pore size, wall thickness and density whereas the functionalization can also be carried out in the graphene sheets that increases the number of covalent bonds between the graphene sheets in the aerogel structure and provides improved mechanical strength. The GA with superior mechanical properties can be

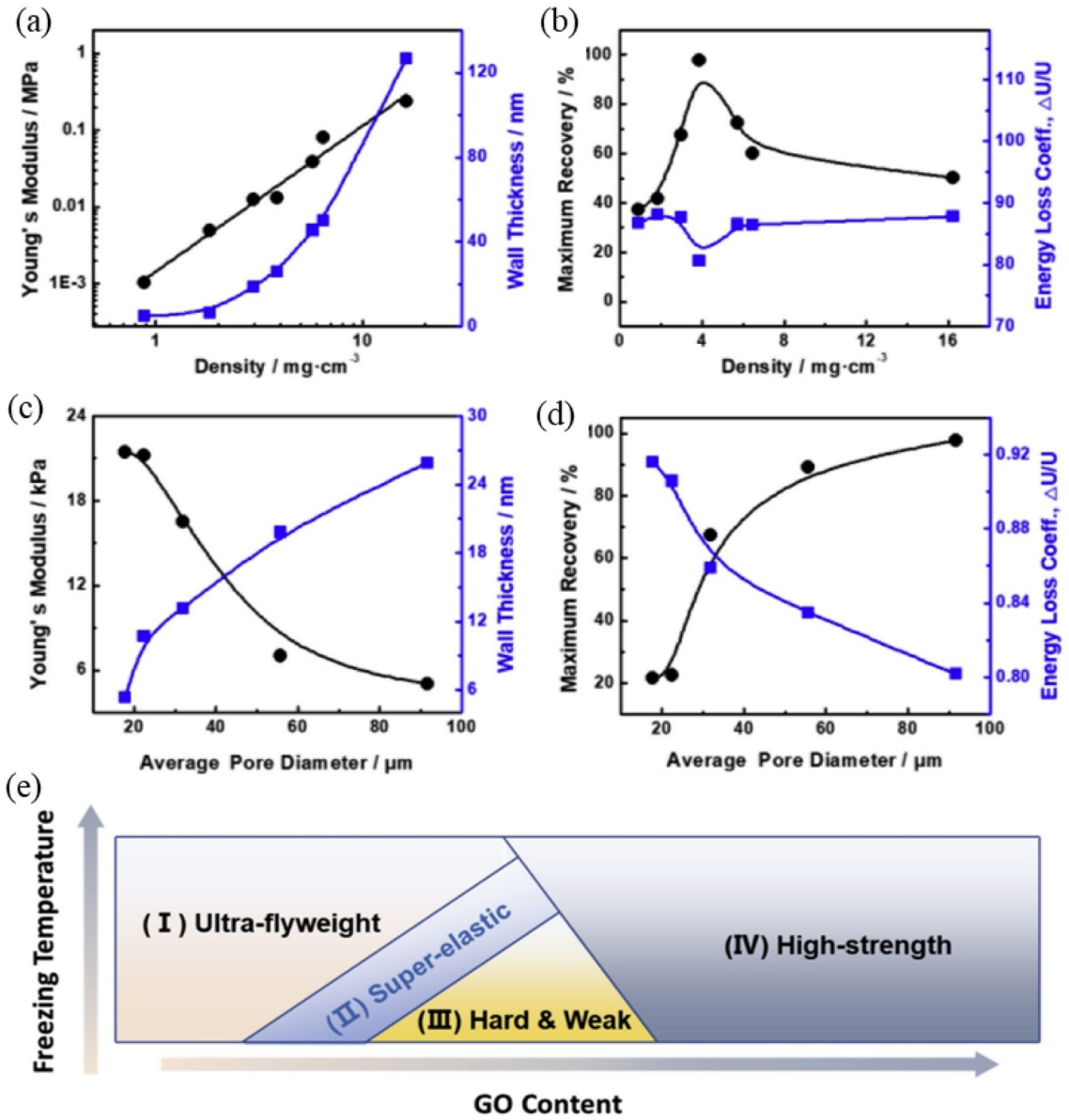

Fig. 3 Effect of density of GA on **a** Young's modulus and wall thickness, **b** maximum recovery and energy loss coefficient. Effect of pore size on the **c** Young's modulus and wall thickness, **d** maximum recovery and energy loss coefficient. **e** Schematic diagram shows the variation in mechanical properties with respect to GO content and freezing temperature. Reproduce with permission [50]

employed either in the form of solid polymer composite or GA modified by polymers for waste-management systems.

3 Synthesis and performance of GA-polymer solid composites

Graphene is a potential reinforcement or nanofiller that can significantly improve the properties of polymer-based composites. However, the poor compatibility of graphene with polymers can cause agglomeration. To disperse pristine graphene in the polymer matrix requires an additional step of chemical modification described in previously published review article [2, 19]. To avoid this additional chemical modification process, GA can be utilized to fabricate polymer-based composites where pores between the graphene sheet network are filled by polymers. The most common method to fabricate GA/polymer composites is infiltration. The process parameters are mostly depending on the physical properties of the polymer matrix [67–69]. Zhang et al.

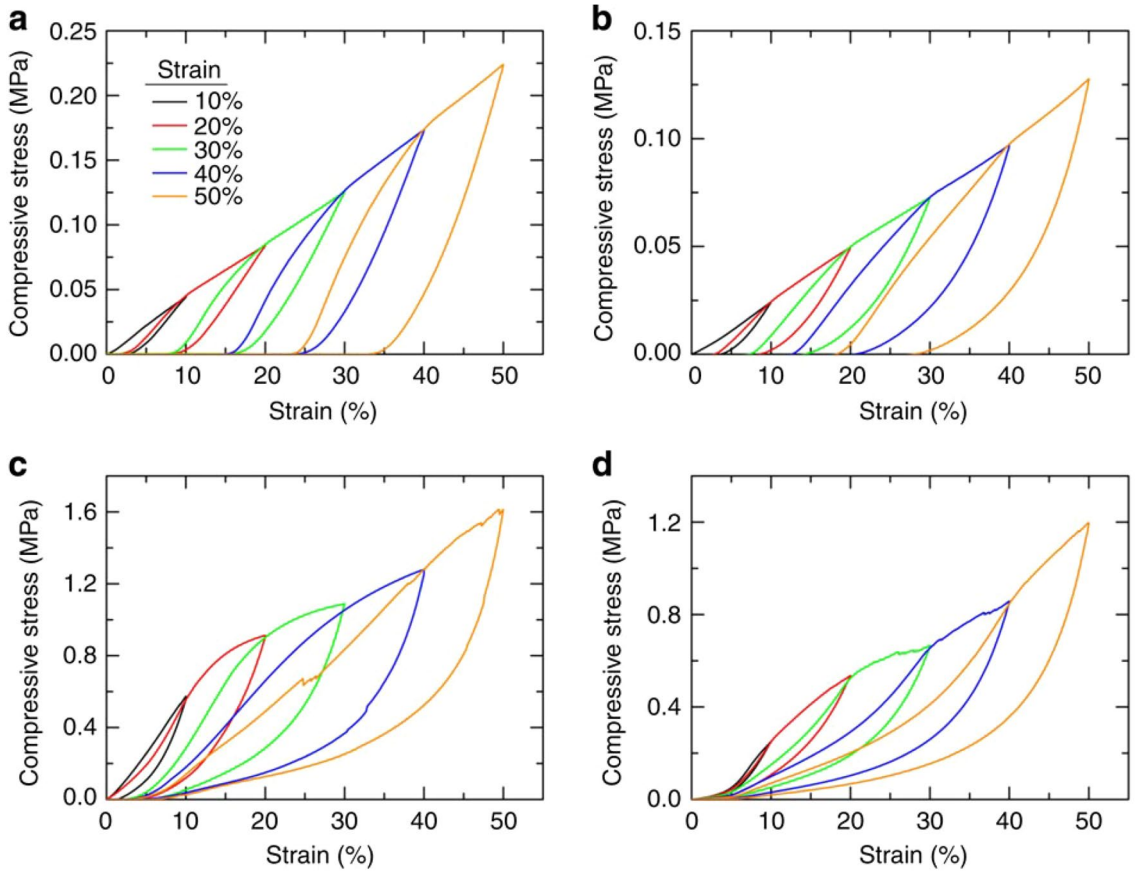

Fig. 4 Compressive stress–strain curves during loading and unloading cycles at different strains for **a** conventional GA, **b** 3D printed GA microlattice using GO ink, **c** conventional GA and **d** 3D printed GA using GO ink with resorcinol and formaldehyde. Reproduce with permission [44]

[67] fabricated GA/polydimethylsiloxane (PDMS) composite by a self-infiltration process. In this process, the authors prepared the PDMS solution by mixing PDMS base agent, curing agent, and n-hexane (10:1:1), and then the solution was magnetically stirred for 30 min. Once the solution was mixed, GA was immersed under the vacuum and ice bath conditions and kept for 6 h to facilitate PDMS penetration into aerogel pores. The good fluidity of PDMS at room temperature ease the process and does not require high temperature. Then, the composite was kept in a vacuum at 55 °C for 5 h to solidify and remove n-hexane. The detailed process is shown in Fig. 5a–c. Figure 5d shows the SEM micrograph of synthesized GA, and mechanical performance evaluated by the compression test is summarized in Fig. 5d. It can be seen that with an increase in GA content in the PDMS, the compressive stress, Young's modulus, and energy density are increased. Moreover, thermal conductivity was also observed to increase with GA content, and the maximum thermal conductivity of 0.58 W/mK for 1 wt% GA composite was measured, which is significantly higher than that of pure PDMS (0.46 W/mK). Using a similar process, Want et al. [69] fabricated the GA/epoxy composite via vacuum infiltration at 60 °C. In this method, firstly, the epoxy resin (LY1556) was diluted with acetone at 10% of epoxy, then curing agent (triethylenetetramine) was added at a weight ratio of 12% of epoxy. After evaporation of acetone in a vacuum oven at room temperature (2 h), the temperature was raised to 60 °C for 30 min to reduce the viscosity of epoxy. GA was immersed into the epoxy solution and degassed in vacuum at 60 °C for 1 h. Finally, the liquid composite was cured at 80 °C for 30 min, followed by post-curing at 110 °C for 2 h. The study suggests that a vacuum can be utilized to infiltrate the GA with viscous polymeric materials. By the same vacuum infiltration technique, Wang et al. [70] synthesized anisotropic GA-epoxy composite with directional electrical conductivities. Anisotropic nature was developed by directional cooling of GO solution during freeze-casting that yielded highly oriented large graphene sheets along the vertical direction bridged by ribbon-like graphene sheets in the transverse direction. The electrical conductivity in parallel direction was one order of magnitude higher than that in transverse direction.

The presence of functional groups in GA has also been advantageous for the in-situ polymerization synthesis

of GA/polymer composite. Li et al. [69] used an in-situ polymerization method to fabricate GA/polyamide composite (Fig. 6). In this process, GA, e-caprolactam (18 g) and 6-aminocaproic acid (2 g) were heated under nitrogen flow to 100 °C for 30 min for repolymerization. Subsequently, the mixture was heated to 180 °C for 1 h and then to 250 °C for 3–4 h until the reactant was completely solidified. After cooling to room temperature, the cylindrical samples were obtained. The authors also compared the electrical conductivity of the composite with other forms for graphene reinforcement in the same matrix, as shown in Fig. 7. The grafting between graphene and polyamide significantly improved electrical conductivity. Other studies on polymer-GA composites are summarized in Table 4 along with corresponding synthesis techniques and properties.

4 Applications

4.1 Oil–water separation

The porous nature of GA makes it a suitable sorbent material for oil–water separation. However, poor mechanical properties of graphene for bulk applications and lesser hydrophobic nature restricts its application. The addition of various polymers in GA has shown excellent capability in terms of compressibility and superior hydrophobic nature for oil–water separation [74–78]. For a successful oil–water separation process, the material should be hydrophobic and oleophilic or vice versa. The polymer-GA composites have been observed to have hydrophobic nature with a high water contact angle that promotes oil absorption. For example, a polyimide-GA composite prepared by freeze-drying and thermal annealing process through the mixing of water-soluble polyimide precursor solution to the GO solution with 1:1 ratio [78]. The absorption capacity of polyimide was in the range of 22.94–37.44 g/g for 10 cycles. The compressibility of the GA provided a consistent absorption capacity over 10 cycles.

Similarly, Zhou et al. [74] prepared the polystyrene-GA composite filled with Fe_3O_4 nanoparticles. Fe_3O_4 nanoparticles were added to magnetize the composite and improves the hydrophobicity. The composite with a volume porosity of 99.7% was able to intake crude oil 10 times of its own mass up to 40 cycles. The 40 wt% Fe_3O_4 increased the water contact angle from 133° to 142°. Furthermore, the incorporation of porous Fe_3O_4 nanoparticles enabled magnetism. The magnetic nature of the composite, in combination with compressibility, made the water cleaning process easier by

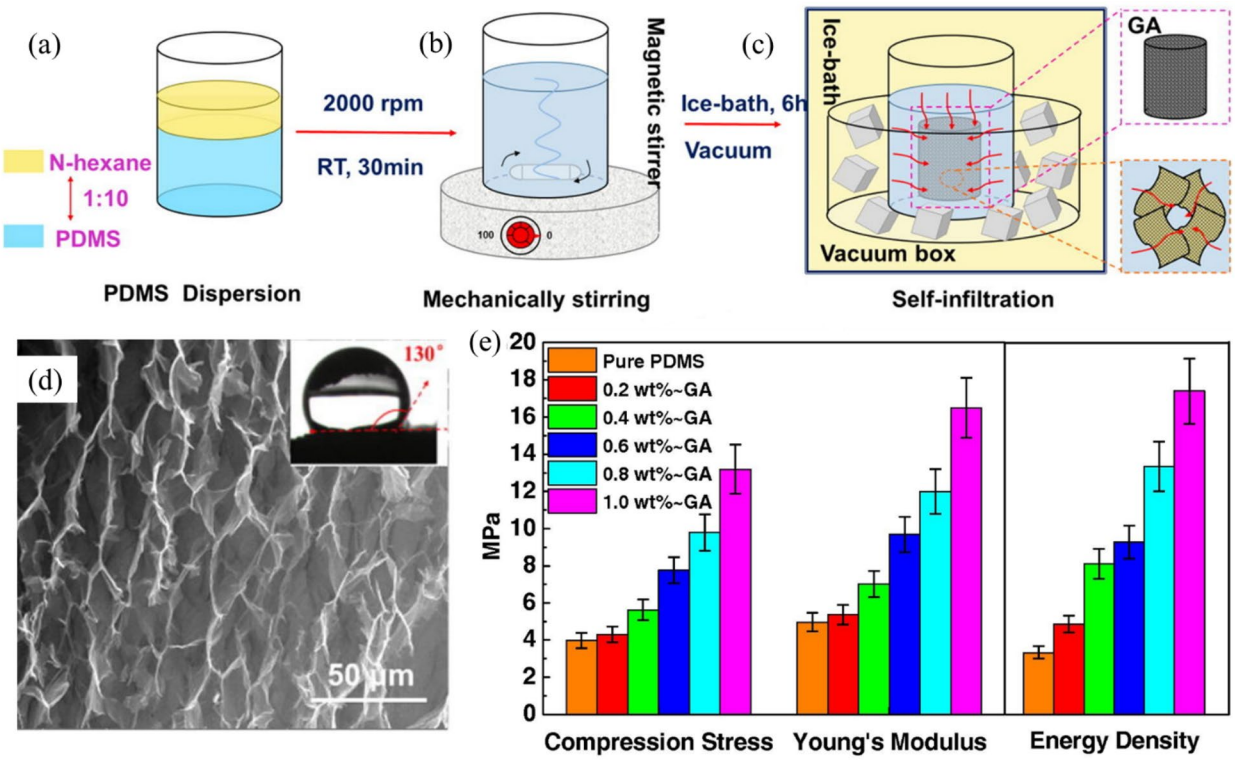

Fig. 5 **a–c** Self-infiltration process for GA/PDMS composite, **d** SEM micrograph of GA framework, and **e** mechanical properties of GA-PDMS composite with different amount of graphene. Reproduce with permission [67]

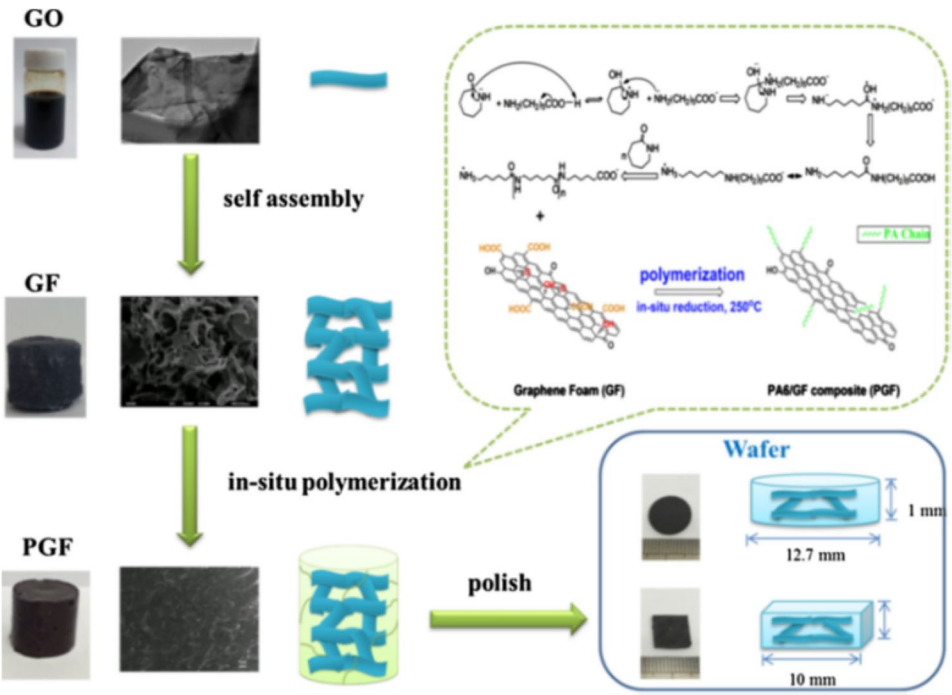

Fig. 6 In-situ polymerization technique to fabricate GA/polyamide composite. Reproduce with permission [69]

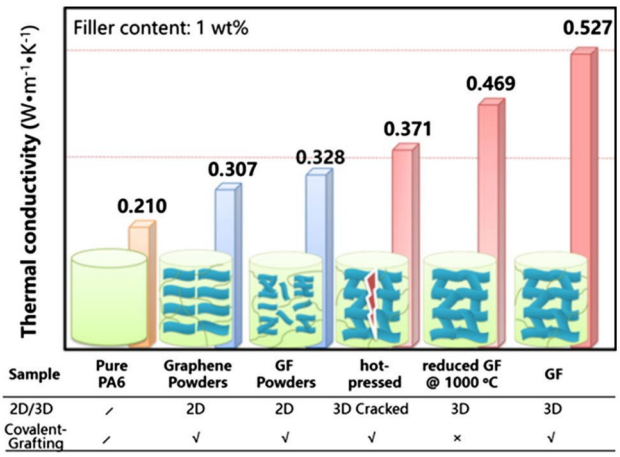

Fig. 7 Comparison of electrical conductivity of polyamide composite reinforced with different forms for graphene. Reproduce with permission [69]

collecting the oil-soaked GA using a magnet and squeezing out the oil. Peanut hull-GA composite has also been studied to evaluate the oil–water separation capacity [77]. Interestingly, this composite from agricultural waste showed excellent absorption capacities of 3820–7933% and superior recyclability (93%) with a water contact angle of 141°.

The absorption capacity of the GA structure also depends on the pore size, which can be controlled by freezing temperature, as explained earlier, using Fig. 2a. The same study also investigated the effect of pore size on absorption capacity. It was found that pore size of ~ 70 µm (freezing temperature of – 20 °C) showed 60% higher weight gain (150 times of its weight) than the pore size of 5.7 µm (freezing temperature of – 196 °C) when absorbing ethanol, acetone, vegetable oil, and Dimethylformamide. The authors suggested that the lower absorption at smaller pores are due to poor pore connectivity that stops the liquid from going through narrow channels inside the GA.

Polymer-GA composites are suitable candidates to replace the existing materials utilized for oil–water separation. For example, different membranes have been developed for oil–water separation, such as copper mesh coated with polytetrafluoroethylene [79], polyacrylamide mesh [80], amphiphilic stainless steel mesh [81], hydrophilic zeolite based membrane [82], etc. However, these mesh or membranes suffers from fouling and weak intrusion pressure that limits their life. Also, these membranes can only filter, it can not store and adsorb the spilled oils. The polymer-GA is superior to the mesh and membrane structures. The other commonly used materials for oil–water separation are mostly super wetting polymeric based porous structures (sponge, foam, and aerogels). The sorption capacity of different polymeric porous materials are available in a review article [83]. The table provided in the review article suggest that the standalone polymeric materials have lower sorption capacity compared to GA-polymeric materials. For example, cellulose aerogels showed sorption capacity in the range

Table 4 Various polymer-GA composites with properties

Matrix-GA	Synthesis technique	Properties	Refs.
PDMS-GA	Self-infiltration	Compressive strain = 80%, electrical conductivity = 1 S/cm, thermal conductivity = 0.58 W/(m K),	[67]
Epoxy-GA	Vacuum infiltration	Electrical conductivity = 67%, Fracture toughness = 113%	[68]
Polyamide-GA	In-situ polymerization + vacuum infiltration	Thermal conductivity = 4 times improved (0.847 W/m/K)	[69]
PDA(polydopamine)-APTS(3-aminopropyltriethoxysilane) / PDMS-GA	Coating + vacuum infiltration	Thermal conductivity = 28.77 W/m/K (in-plane) and 1.62 W/m/K (out-of-plane)	[71]
PMMA (poly methyl methacrylate)-GA	In-situ polymerization + infiltration	With 2.5 vol.%, Vickers hardness = 462 MPa (pure PMMA = 205 MPa), Thermal conductivity = 0.7 W/K/m (pure PMMA = 0.2 W/K/m)	[72]
Copper nanowire-GA/Epoxy	Freeze drying + thermal annealing + infiltration	Thermal conductivity coefficient, λ = 0.51 for the composites Cu nanowire (6 wt%) and GA (1.2 wt%). For pure epoxy, λ = 0.21	[73]

of 80–185 wt/wt, which increased to 197 wt/wt in case of cellulose/GA composite. Therefore, the utilization of GA-polymer composites will be beneficial.

4.2 Water cleaning by absorbing ions and organic matter

GA has also been utilized for cleaning water. GA prepared by reduction of GO solution using vitamin C resulted in a hydrophobic GA structure after freeze-drying [92]. The adsorption capacity of the prepared GA is 138–328 times of its own weight; it can absorb organic liquids, including alcohols, alkane, mineral oil, vegetable oil, etc. The adsorption capacity of this GA reduced by vitamin C is shown in Fig. 8.

In addition to the hydrophobicity of GA, electrochemical nature can also be utilized to remove or degrade pollutants from wastewater by using GA electrodes. Chen et al. [93] developed nitrogen-doped GA particle electrode to degrade Bisphenol A (BPA), which is an environmental harmful organic pollutant. A three-electrode reactor was used where a stainless steel and copper wire were used as main anode and cathode, respectively. Nitrogen-doped GA sample was first saturated by BPA solution then transferred into anode reaction zone to form a three-dimensional electrode. After applying 20 V of DC power supply, every particle in the GA got polarized and acted as a cathode on one side and anode on the other side. Thus, the degradation of BPA occurred. The degradation rate of BPA was observed to be 90% after 30 min of water treatment with BPA concentration of 15 mg/L. Similar to electrochemical degradation of BPA, GA can also be for photocatalytic degradation of aromatic organic dyes along with photooxidative agent Ag_3PO_4 [94]. First, the hydrogel was prepared by GO and $AgNO_3$ solution (15 mL, 0.4 mmol). During the hydrogel process, Ag nanoparticles started nucleating and growing on the GO surfaces. The prepared hydrogel was washed with distilled water followed by immersion into silver-ammino ($[Ag(NH_3)_2]^+$) aqueous solution (0.2 M) for 4 h. Then, it was again immersed into Na_2HPO_4 aqueous solution (0.15 M) for another 24 h. Finally, the Ag/Ag_3PO_4/GA was prepared by freeze-drying of resulted hydrogel. The resulted Ag/Ag_3PO_4/GA composite aerogel was able to eliminate cationic and anionic dyes and maintained consistent degradation efficiency of even after 6 cycles, whereas the Ag_3PO_4/GO catalyze showed only 20% of degradation efficiency after 6 cycles. During photocatalytic degradation, GA does not only provide higher surface area, but it also enhances the separation and transfer of photoexcited charge carriers due to inherent nature of graphene.

4.3 Other applications

GA and its porous composites have several other applications such as photocatalyst, biosensors, supercapacitors, electrocatalyst, lithium-ion battery, thermal management, and fuel cell, etc. These different applications are listed in Table 5 and compared with other suitable materials. For example, the photocatalyst application for adsorption such as methyl orange (MO), GA- Graphitic carbon nitride ($g\text{-}C_3N_4$) show higher degradation efficiency than the $g\text{-}C_3N_4/Ag_2O$ composite material. GA can also be used as electrochemical sensors because of its electronic/ionic conductivity. The tribological application of GA/TiO_2 composite has also been investigated in dry and oil lubricated condition [95]. The

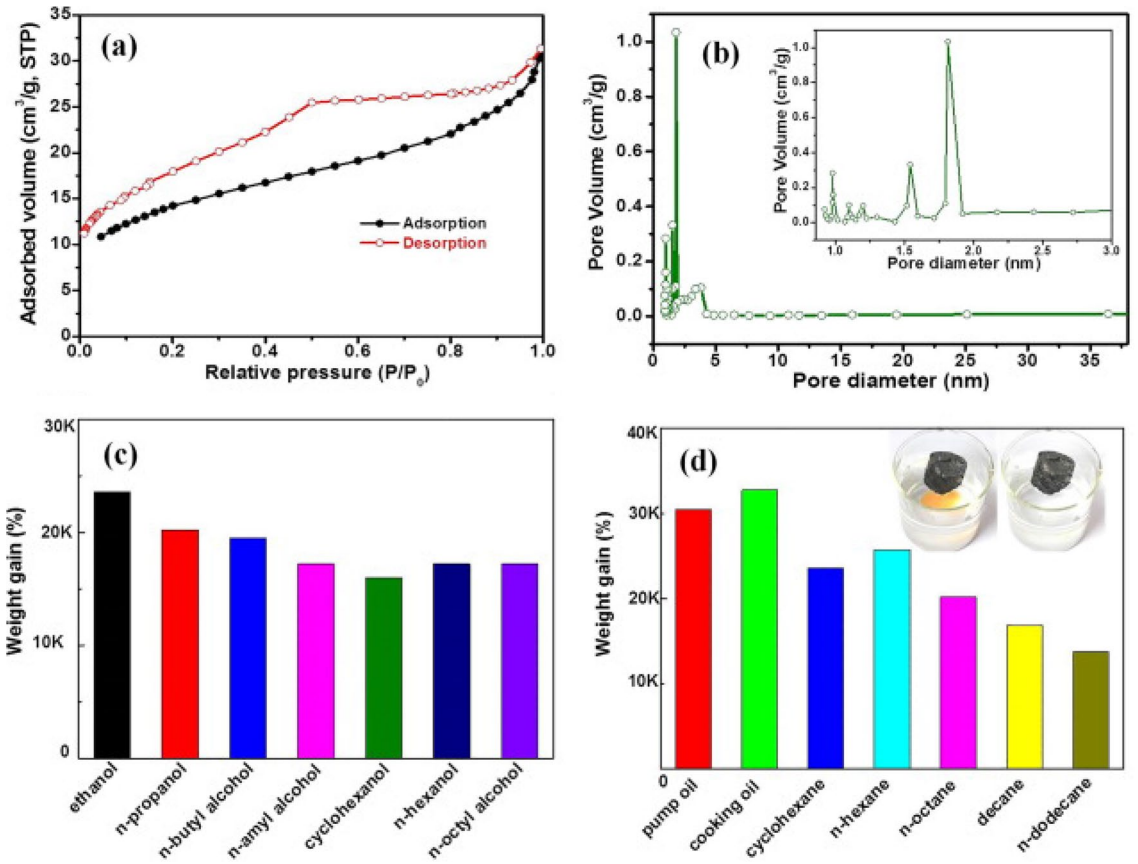

Fig. 8 Adsorption capacity of GA: **a** adsorption–desorption isotherm, **b** desorption pore size distribution, **c** and **d** % gain by adsorbing various organic liquids. Reproduce with permission [92]

composite were prepared by infiltration of TiO_2 into the GA where the GA was synthesized using sol–gel method with different concentration of graphene (5, 7 and 9 mg/mL). After infiltration, the GA/TiO_2 was compressed in two steps—first at 5 MPa for 30 min then 10 MPa for 30 min. The compressed composites were sintered at 700 °C for 2 h. The tribological tests at dry condition at 5 N and 5 mm/s sliding velocity showed that the mean value of coefficient of friction (COF) decreases from 0.3 to 0.18 with increase in graphene concentration from 5 mg/mL. The lower COF at higher graphene content is attributed to self-lubricating phenomena of graphene [96]. Whereas, the COF further decreased in oil lubricated condition in the range of 0.17 to 0.12. Prior to tribological tests in oil lubricated condition, the composites were immersed in the oil for 24 h to absorb oil in the pores. It is expected that the observed oil in the pores of the composites transported to the interface during sliding due to capillary action.

For CO_2 separation, the usage of GA with ionic liquid has been evaluated. The infiltration of ionic liquid (1-N-butyl-3-methylimidazolium hexafluorophosphate) to the GA with 50% loading has shown CO_2/CH_4 separation improved by 20 times compared to GA without any ionic liquid [97]. The ionic moieties of the IL is the primary source for CO_2 capture. The pristine GA does not have any ionic moieties to participate in CO_2 capture directly. However, it was proposed that the molecular interaction between reduced graphene layers and anion of the ionic liquid improves the separation capacity, and it can be further enhanced by tuning the GA surface, selection of ionic liquid, and N doping in the GA [98]. Similarly, some other capabilities of the GA and its composites in various fields are highlighted in the Table 5. The different entries in Table 5 also suggest that GA can be easily tuned by the addition of suitable materials for different applications.

5 Conclusions

GA with excellent mechanical properties, mainly compressibility, enables to utilize the properties of 2D graphene sheet for a component rather than as an additive. The properties of GA and its composites can be tailored during synthesis. The common synthesis techniques for GA are hydrothermal

Table 5 Comparison of GA performance for different applications

Application	GA or GA composites	Other suitable material	Assessment
Photocatalyst (Methlyl orange, MO degradation)	Graphitic carbon nitride (g-C_3N_4)-GA composite, degradation efficiency = 92% 4 h, MO = 20 mg/mL [99]	g-C_3N_4/Ag_2O composite, degradation efficiency = 80% 30 min, MO = 20 mg/mL^{-1} [100]	Higher degradation efficiency of GA based composite
Aerocapacitor	Thionine functionalized GA, specific power = 12.8 kW/kg [101]	Carbon aerogel, specific power = 7.5 kW/kg [102]	Functionalized GA has higher specific power than the carbon aerogel
Electrode for dye sensitized solar cell (DSSC)	Polyaniline nanotube-GA, efficiency = 5.47%, current density = 11.5 mA/cm^2 [103]	TiO_2 aerogel-metal organic framework nanocomposite, efficiency = 5.47%, current density = 11.5 mA/cm^2 [104]	Although the TiO_2 aerogel was used as a photoanode and GA based electrode used as a counter electrode in their respective DSSC, still GA showed potential for solar cells
Electrical applications (electrode for batteries and capacitors)	GA, Electrical conductivity = 87 S/m [105]	Silver nanowire aerogel, electrical conductivity = 51,000 S/m [106], copper nanowire aerogel, electrical conductivity = 11,600 S/m [107]	Although the metal aerogels have higher conductivity, but GA is cost effective which can be easily employed for electrical applications
Biosensors (dopamine detection ability)	Palladium-gold nanoalloys/nitrogen and sulphur-functionalized GA, dopamine concentration range = 0.001–100 µM, detection limit = 0.00036 µM [108]	Hierarchical nanoporous PtTi alloy, dopamine concentration range = 4–500 µM, detection limit = 3.2 µM [109]	GA based composite material can detect dopamine for larger concentration range with a lower detection limit
Electrocatalyst (methanol electrooxidation)	Pt/C/GA composite catalyst, After 1000 cycles of voltammetry cycles, 16% of initial mass activity lost	Pt/C catalyst, After 1000 cycles of voltammetry cycles, 40% of initial mass activity lost [110]	Pt/C/GA catalyst showed higher mass activity for methanol electrooxidation
Thermal management (phase change composites)	Polyethylene glycol (PEG)/cellulose/GA, latent heat of fusion = 156.1 J/g [111]	PEG/cellulose, latent heat of fusion = 91.8 J/g [112]	Graphene provided higher thermal conductivity to the GA composite for improved thermal management
Cathode material for $LiFePO_4$ battery	$LiFePO_4$/GA, specific capacity = 167 mAh/g (at 10 °C) and Li + diffusion coefficient = 3.23×10^{-13} cm^2/s [113]	$LiFePO_4$/graphene sheet, specific capacity = 160 mAh/g (at 10 °C) and Li + diffusion coefficient = 6.77×10^{-13} cm^2/s [113]	Graphene network in GA provides abundant path for ion/electro movement and open pores work as electrolyte storage for fast supply of Li^+

and 3D printing, followed by the freeze-drying process. Both processes require a precursor solution of GO. However, the hydrothermal process is an easy and convenient process, and it can also be used for large scale production of GA. Other than the convenient nature of the hydrothermal process, it also reduces the GO by cross-linking of GO sheets, and the additional step of thermal reduction can be avoided. The reduced graphene hydrogel after the hydrothermal process requires a freeze-drying step where the aqueous solution freezes and sublimates to form GA. The concentration of GO solution and freezing temperature are important parameters to control the morphology of GA. Generally, a decrease in freezing temperature reduces the pore size and improves the mechanical properties of GA. The 3D printing of GA is sophisticated, but it provides an advantage of having lower GO concentration of the printing ink that leads to the higher surface area in the resulted GA with higher recovery under compressive loading.

The superior mechanical properties of the GA, along with the inherent properties of graphene, led to its application in various electrical, electrochemical devices in the form of solid GA-polymer composite or GA modified by polymers. The solid GA-polymer composites overcome the agglomeration problem when graphene sheets added in the polymer matrix. Also, the solid GA-polymer composites by the infiltration method show exceptional mechanical properties with other desired properties such as electrical conductivity. It is also worth mentioning that the initial morphology of the GA can assist in building polymer composites with anisotropic structure.

The GA is inherently oleophilic and hydrophobic that enable oil–water separation and organic pollutant removal from water. To further enhance the mechanical stability of the GA for reusability of GA, GA has been modified with different polymeric materials such as polyvinylidene fluoride, chitosan, polystyrene, etc. These polymeric agents have also been observed to improve hydrophobicity that enhances the water-cleaning capacity of the GA. Other than mechanical and hydrophobic properties, GA possesses several other remarkable properties that make it versatile to be employed in different applications.

Acknowledgements Not applicable.

Author contributions AKK and ST wrote the manuscript. GX and PLM supervised the conception. All the authors read and approved the final manuscript.

Funding Authors acknowledge the startup funding from Mechanical Engineering Department, University of Nevada, Reno. G. Xiong gratefully acknowledges financial supports from the University of Texas at Dallas startup fund and the National Science Foundation (Grant No. CMMI1923033).

Data availability Data sharing is not applicable to this article as no data were generated during the critical review.

Declarations

Conflict of interest The authors declare that they have no competing interests.

References

1. K.S. Novoselov, A.K. Geim, S.V. Morozov, D. Jiang, Y. Zhang, S.V. Dubonos, I.V. Grigorieva, A.A. Firsov, Science (80-.) **306**, 666 (2004)
2. A.K. Kasar, P.L. Menezes, Int. J. Adv. Manuf. Technol. **97**, 3999 (2018)
3. H.C. Lee, W.-W. Liu, S.-P. Chai, A.R. Mohamed, A. Aziz, C.-S. Khe, N.M.S. Hidayah, U. Hashim, RSC Adv. **7**, 15644 (2017)
4. C. Lee, X. Wei, J.W. Kysar, J. Hone, Science (80-.) **321**, 385 (2008)
5. S. Ghosh, I. Calizo, D. Teweldebrhan, E.P. Pokatilov, D.L. Nika, A.A. Balandin, W. Bao, F. Miao, C.N. Lau, Appl. Phys. Lett. **92**, 151911 (2008)
6. Copper Annealed (MatWeb Materials Property Data) https://www.matweb.com/search/datasheet.aspx?matguid=9aebe83845c04c1db5126fada6f76f7e&ckck=1. Accessed 20 Jan 2021
7. Z. Qin, M. Taylor, M. Hwang, K. Bertoldi, M.J. Buehler, Nano Lett. **14**, 6520 (2014)
8. A. Raichura, M. Dutta, M.A. Stroscio, Phys. Status Solidi **241**, 3448 (2004)
9. ASTM A36 Steel (MatWeb Materials Property Data) https://www.matweb.com/search/DataSheet.aspx?MatGUID=afc003f4fb40465fa3df05129f0e88e6&ckck=1. Accessed 20 Jan 2021
10. M.D. Stoller, S. Park, Y. Zhu, J. An, R.S. Ruoff, Nano Lett. **8**, 3498 (2008)
11. S. Zhang, M. Zheng, Z. Lin, N. Li, Y. Liu, B. Zhao, H. Pang, J. Cao, P. He, Y. Shi, J. Mater. Chem. A **2**, 15889 (2014)
12. R.R. Nair, P. Blake, A.N. Grigorenko, K.S. Novoselov, T.J. Booth, T. Stauber, N.M.R. Peres, A.K. Geim, Science (80-.) **320**, 1308 (2008)
13. A.H. Ali, Z. Hassan, A. Shuhaimi, Appl. Surf. Sci. **443**, 544 (2018)
14. R. Murali, Y. Yang, K. Brenner, T. Beck, J.D. Meindl, Appl. Phys. Lett. **94**, 243114 (2009)
15. G. Schindler, G. Steinlesberger, M. Engelhardt, W. Steinhögl, Solid State Electron. **47**, 1233 (2003)
16. M. Dragoman, D. Dragoman, Prog. Quantum Electron. **33**, 165 (2009)
17. L.-C. Xu, A. Du, L. Kou, Phys. Chem. Chem. Phys. **18**, 27284 (2016)
18. R. Jiang, X. Zhou, Q. Fang, Z. Liu, Mater. Sci. Eng. A **654**, 124 (2016)
19. A.K. Kasar, G. Xiong, P.L. Menezes, JOM **70**, 829 (2018)
20. Y. Kim, J. Lee, M.S. Yeom, J.W. Shin, H. Kim, Y. Cui, J.W. Kysar, J. Hone, Y. Jung, S. Jeon, Nat. Commun. **4**, 2114 (2013)
21. S.-L. Chou, J.-Z. Wang, M. Choucair, H.-K. Liu, J.A. Stride, S.-X. Dou, Electrochem. Commun. **12**, 303 (2010)
22. J.L. Gurav, I.-K. Jung, H.-H. Park, E.S. Kang, D.Y. Nadargi, J. Nanomater. **2010**, 1–11 (2010)
23. R. Kumar, S. Sen Gupta, S. Katiyar, V.K. Raman, S.K. Varigala, T. Pradeep, A. Sharma, Carbon N. Y. **99**, 375 (2016)
24. P. He, X. Qian, Z. Fei, Q. Liu, Z. Zhang, X. Chen, J. Tang, M. Cui, X. Qiao, Processes **6**, 35 (2018)

25. H. Hirashima, C. Kojima, H. Imai, J. Sol-Gel Sci. Technol. **8**, 843 (1997)
26. F. Cao, L. Ren, X. Li, RSC Adv. **5**, 18025 (2015)
27. J.F. Poco, J.H. Satcher Jr., L.W. Hrubesh, J. Non Cryst. Solids **285**, 57 (2001)
28. S. Alwin, X. Sahaya Shajan, R. Menon, P.Y. Nabhiraj, K.G.K. Warrier, G. Mohan Rao, Thin Solid Films **595**, 164 (2015)
29. X. Wang, C. Li, Z. Shi, M. Zhi, Z. Hong, RSC Adv. **8**, 8011 (2018)
30. S. Yoon, G.D. Han, D.Y. Jang, J.W. Kim, D.H. Kim, J.H. Shim, J. Alloys Compd. **806**, 1430 (2019)
31. C.-C. Lin, T.-Y. Wei, K.-T. Lee, S.-Y. Lu, J. Mater. Chem. **21**, 12668 (2011)
32. T. Long, Y. Xu, X. Lv, J. Ran, S. Yang, L. Xu, Mater. Des. **159**, 195 (2018)
33. T. Fu, J. Tang, K. Chen, F. Zhang, Appl. Opt. **55**, 705 (2016)
34. H. Suo, W. Wang, S. Jiang, Y. Li, K. Yu, S. Huang, S. Cui, X. Shen, J. Xue, SN Appl. Sci. **1**, 461 (2019)
35. Y. Xu, K. Sheng, C. Li, G. Shi, ACS Nano **4**, 4324 (2010)
36. Y. Wu, N. Yi, L. Huang, T. Zhang, S. Fang, H. Chang, N. Li, J. Oh, J.A. Lee, M. Kozlov, Nat. Commun. **6**, 1 (2015)
37. C. Wang, X. He, Y. Shang, Q. Peng, Y. Qin, E. Shi, Y. Yang, S. Wu, W. Xu, S. Du, J. Mater. Chem. A **2**, 14994 (2014)
38. W. Liao, H.-B. Zhao, Z. Liu, S. Xu, Y.-Z. Wang, Compos. Part B Eng. **173**, 107036 (2019)
39. X. Zhu, C. Yang, P. Wu, Z. Ma, Y. Shang, G. Bai, X. Liu, G. Chang, N. Li, J. Dai, Nanoscale **12**, 4882 (2020)
40. W. Chen, L. Yan, Nanoscale **3**, 3132 (2011)
41. M.A. Worsley, T.T. Pham, A. Yan, S.J. Shin, J.R.I. Lee, M. Bagge-Hansen, W. Mickelson, A. Zettl, ACS Nano **8**, 11013 (2014)
42. Q. Zhang, F. Zhang, S.P. Medarametla, H. Li, C. Zhou, D. Lin, Small **12**, 1702 (2016)
43. Y. Jiang, Z. Xu, T. Huang, Y. Liu, F. Guo, J. Xi, W. Gao, C. Gao, Adv. Funct. Mater. **28**, 1707024 (2018)
44. C. Zhu, T.Y.-J. Han, E.B. Duoss, A.M. Golobic, J.D. Kuntz, C.M. Spadaccini, M.A. Worsley, Nat. Commun. **6**, 6962 (2015)
45. M.A. Riaz, P. Hadi, I.H. Abidi, A. Tyagi, X. Ou, Z. Luo, RSC Adv. **7**, 29722 (2017)
46. W. Gao, N. Zhao, W. Yao, Z. Xu, H. Bai, C. Gao, RSC Adv. **7**, 33600 (2017)
47. Y. Qin, Q. Peng, Y. Ding, Z. Lin, C. Wang, Y. Li, F. Xu, J. Li, Y. Yuan, X. He, ACS Nano **9**, 8933 (2015)
48. M. Yang, N. Zhao, Y. Cui, W. Gao, Q. Zhao, C. Gao, H. Bai, T. Xie, ACS Nano **11**, 6817 (2017)
49. Z. Han, Z. Tang, P. Li, G. Yang, Q. Zheng, J. Yang, Nanoscale **5**, 5462 (2013)
50. X. Liu, K. Pang, H. Yang, X. Guo, Carbon N. Y. **161**, 146 (2020)
51. C. Zhu, T. Liu, F. Qian, T.Y.-J. Han, E.B. Duoss, J.D. Kuntz, C.M. Spadaccini, M.A. Worsley, Y. Li, Nano Lett. **16**, 3448 (2016)
52. X. Tang, H. Zhou, Z. Cai, D. Cheng, P. He, P. Xie, D. Zhang, T. Fan, ACS Nano **12**, 3502 (2018)
53. L. Lv, P. Zhang, H. Cheng, Y. Zhao, Z. Zhang, G. Shi, L. Qu, Small **12**, 3229 (2016)
54. S.J. Yeo, M.J. Oh, H.M. Jun, M. Lee, J.G. Bae, Y. Kim, K.J. Park, S. Lee, D. Lee, B.M. Weon, Adv. Mater. **30**, 1802997 (2018)
55. H. Yang, Z. Li, B. Lu, J. Gao, X. Jin, G. Sun, G. Zhang, P. Zhang, L. Qu, ACS Nano **12**, 11407 (2018)
56. L. Qiu, J.Z. Liu, S.L.Y. Chang, Y. Wu, D. Li, Nat. Commun. **3**, 1 (2012)
57. Y. Li, J. Chen, L. Huang, C. Li, J. Hong, G. Shi, Adv. Mater. **26**, 4789 (2014)
58. C. Wu, X. Huang, X. Wu, R. Qian, P. Jiang, Adv. Mater. **25**, 5658 (2013)
59. H. Hu, Z. Zhao, W. Wan, Y. Gogotsi, J. Qiu, Adv. Mater. **25**, 2219 (2013)
60. B. Yao, J. Chen, L. Huang, Q. Zhou, G. Shi, Adv. Mater. **28**, 1623 (2016)
61. H.-L. Gao, Y.-B. Zhu, L.-B. Mao, F.-C. Wang, X.-S. Luo, Y.-Y. Liu, Y. Lu, Z. Pan, J. Ge, W. Shen, Nat. Commun. **7**, 1 (2016)
62. Y. Lin, F. Liu, G. Casano, R. Bhavsar, I.A. Kinloch, B. Derby, Adv. Mater. **28**, 7993 (2016)
63. X. Xu, Q. Zhang, Y. Yu, W. Chen, H. Hu, H. Li, Adv. Mater. **28**, 9223 (2016)
64. C. Hu, J. Xue, L. Dong, Y. Jiang, X. Wang, L. Qu, L. Dai, ACS Nano **10**, 1325 (2016)
65. H. Huang, P. Chen, X. Zhang, Y. Lu, W. Zhan, Small **9**, 1397 (2013)
66. Q. Zhang, X. Xu, D. Lin, W. Chen, G. Xiong, Y. Yu, T.S. Fisher, H. Li, Adv. Mater. **28**, 2229 (2016)
67. Q. Zhang, X. Xu, H. Li, G. Xiong, H. Hu, T.S. Fisher, Carbon N. Y. **93**, 659 (2015)
68. Z. Wang, X. Shen, M. Akbari Garakani, X. Lin, Y. Wu, X. Liu, X. Sun, J.-K. Kim, ACS Appl. Mater. Interfaces **7**, 5538 (2015)
69. X. Li, L. Shao, N. Song, L. Shi, P. Ding, Compos. Part A Appl. Sci. Manuf. **88**, 305 (2016)
70. Z. Wang, X. Shen, N.M. Han, X. Liu, Y. Wu, W. Ye, J.-K. Kim, Chem. Mater. **28**, 6731 (2016)
71. H. Fang, Y. Zhao, Y. Zhang, Y. Ren, S.-L. Bai, ACS Appl. Mater. Interfaces **9**, 26447 (2017)
72. Z. Fan, F. Gong, S.T. Nguyen, H.M. Duong, Carbon N. Y. **81**, 396 (2015)
73. X. Yang, S. Fan, Y. Li, Y. Guo, Y. Li, K. Ruan, S. Zhang, J. Zhang, J. Kong, J. Gu, Compos. Part A Appl. Sci. Manuf. **128**, 105670 (2020)
74. S. Zhou, W. Jiang, T. Wang, Y. Lu, Ind. Eng. Chem. Res. **54**, 5460 (2015)
75. N. Cao, Q. Lyu, J. Li, Y. Wang, B. Yang, S. Szunerits, R. Boukherroub, Chem. Eng. J. **326**, 17 (2017)
76. S. Yang, C. Shen, L. Chen, C. Wang, M. Rana, P. Lv, ACS Appl. Nano Mater. **1**, 531 (2018)
77. N. Li, Q. Yue, B. Gao, X. Xu, R. Su, J. Clean. Prod. **207**, 764 (2019)
78. R.-P. Ren, Z. Wang, J. Ren, Y.-K. Lv, J. Mater. Sci. **54**, 5918 (2019)
79. L. Feng, Z. Zhang, Z. Mai, Y. Ma, B. Liu, L. Jiang, D. Zhu, Angew. Int. Ed. **43**, 2012 (2014)
80. Z. Xue, S. Wang, L. Lin, L. Chen, M. Liu, L. Feng, L. Jiang, Adv. Mater. **23**, 4270 (2011)
81. G.J. Dunderdale, M.W. England, T. Sato, C. Urata, A. Hozumi, Macromol. Mater. Eng. **301**, 1032 (2016)
82. J. Guo, Z. Ji, Colloids Surf. A Physicochem. Eng. Asp. **595**, 124727 (2020)
83. Y. Guan, F. Cheng, Z. Pan, Polymers **11**, 806 (2019)
84. R. Li, C. Chen, J. Li, L. Xu, G. Xiao, D. Yan, J. Mater. Chem. A **2**, 3057 (2014)
85. J. Xiao, W. Lv, Y. Song, Q. Zheng, Chem. Eng. J. **338**, 202 (2018)
86. L. Xu, G. Xiao, C. Chen, R. Li, Y. Mai, G. Sun, D. Yan, J. Mater. Chem. A **3**, 7498 (2015)
87. Y. Li, H. Zhang, M. Fan, P. Zheng, J. Zhuang, L. Chen, Sci. Rep. **7**, 46379 (2017)
88. C. Wang, S. Yang, Q. Ma, X. Jia, P.-C. Ma, Carbon N. Y. **118**, 765 (2017)
89. C. Chen, F. Li, Y. Zhang, B. Wang, Y. Fan, X. Wang, R. Sun, Chem. Eng. J. **350**, 173 (2018)
90. Y. Bo, A. Yu, H. Liu, S. Chen, W. Xu, S. Diao, C. Zhang, J. Porous Mater. **28**, 39 (2021)
91. K. Ji, Y. Gao, L. Zhang, S. Wang, Q. Yue, X. Xu, W. Kong, B. Gao, Z. Cai, Y. Chen, Sci. Total Environ. **763**, 142958 (2021)

92. S. Dong, L. Xia, T. Guo, F. Zhang, L. Cui, X. Su, D. Wang, W. Guo, J. Sun, Appl. Surf. Sci. **445**, 30 (2018)
93. Z. Chen, Y. Zhang, L. Zhou, H. Zhu, F. Wan, Y. Wang, D. Zhang, J. Hazard. Mater. **332**, 70 (2017)
94. F. Chen, S. Li, Q. Chen, X. Zheng, P. Liu, S. Fang, Mater. Res. Bull. **105**, 334 (2018)
95. P. Huang, R. Zhu, C. Li, X. Wang, X. Wang, X. Zhang, Mater. Des. **188**, 108468 (2020)
96. E. Omrani, A.D. Moghadam, A.K. Kasar, P. Rohatgi, P.L. Menezes, Materials (Basel) **14**, 1183 (2021)
97. M. Zeeshan, K. Yalcin, F.E. Sarac Oztuna, U. Unal, S. Keskin, A. Uzun, Carbon N. Y. **171**, 79 (2021)
98. A. Pruna, A.C. Cárcel, A. Benedito, E. Giménez, Appl. Surf. Sci. **487**, 228 (2019)
99. Z. Tong, D. Yang, J. Shi, Y. Nan, Y. Sun, Z. Jiang, ACS Appl. Mater. Interfaces **7**, 25693 (2015)
100. M. Xu, L. Han, S. Dong, ACS Appl. Mater. Interfaces **5**, 12533 (2013)
101. Y. Shabangoli, M.S. Rahmanifar, M.F. El-Kady, A. Noori, M.F. Mousavi, R.B. Kaner, Adv. Energy Mater. **8**, 1802869 (2018)
102. S.T. Mayer, R.W. Pekala, J.L. Kaschmitter, J. Electrochem. Soc. **140**, 446 (1993)
103. K. Mohan, A. Bora, R.S. Roy, B.C. Nath, S.K. Dolui, Sol. Energy **186**, 360 (2019)
104. S. Alwin, V. Ramasubbu, X.S. Shajan, Bull. Mater. Sci. **41**, 27 (2018)
105. M.A. Worsley, P.J. Pauzauskie, T.Y. Olson, J. Biener, J.H. Satcher Jr., T.F. Baumann, J. Am. Chem. Soc. **132**, 14067 (2010)
106. F. Qian, P.C. Lan, M.C. Freyman, W. Chen, T. Kou, T.Y. Olson, C. Zhu, M.A. Worsley, E.B. Duoss, C.M. Spadaccini, Nano Lett. **17**, 7171 (2017)
107. S.M. Jung, D.J. Preston, H.Y. Jung, Z. Deng, E.N. Wang, J. Kong, Adv. Mater. **28**, 1413 (2016)
108. R. Li, T. Yang, Z. Li, Z. Gu, G. Wang, J. Liu, Anal. Chim. Acta **954**, 43 (2017)
109. D. Zhao, G. Yu, K. Tian, C. Xu, Biosens. Bioelectron. **82**, 119 (2016)
110. L. Zhao, Z.-B. Wang, J.-L. Li, J.-J. Zhang, X.-L. Sui, L.-M. Zhang, Electrochim. Acta **189**, 175 (2016)
111. J. Yang, E. Zhang, X. Li, Y. Zhang, J. Qu, Z.-Z. Yu, Carbon N. Y. **98**, 50 (2016)
112. S.B. Şentürk, D. Kahraman, C. Alkan, İ Gökçe, Carbohydr. Polym. **84**, 141 (2011)
113. X. Tian, Y. Zhou, X. Tu, Z. Zhang, G. Du, J. Power Sources **340**, 40 (2017)